ADVANCED MATERIALS
www.advmat.de

Revealing the Neglected Role of Passivation Layers of Current Collectors for Solid-State Anode-Free Batteries

Yijia Wang, Bibin Jose, Yi Yuan, Aadharshini Ganesh, Rina Muhammad Faisal, Ka Ho Chan, Jack Bekou, Lijia Liu, Payam Kaghazchi, and Yang Zhao**

Anode-free sulfide-based all-solid-state lithium metal batteries (ASSLMBs), which eliminate the need for a lithium metal anode during fabrication, offer superior energy density, enhanced safety, and simplified manufacturing. Their performance is largely influenced by the interfacial properties of the current collectors. Although previous studies have investigated the degradation of sulfide electrolytes on commonly used copper (Cu) and stainless steel (SS) current collectors, the impact of spontaneously formed surface oxides, such as copper oxide (Cu_2O/CuO) and chromium oxide (Cr_2O_3), on interfacial stability remains underexplored. This study systematically evaluates the neglected role of passivation layers of both Cu and SS. Results demonstrate that Cu facilitates more stable lithium deposition. Electrochemical impedance spectroscopy (EIS) reveals that interfacial resistance on SS is consistently higher than on Cu during cycling. In-situ X-ray absorption spectroscopy (XAS) and computational modelling confirm the formation of phosphate (PO_4^{3-}) and sulfate (SO_4^{2-}) species at both interfaces, attributed to reactions between the sulfide electrolyte and surface oxides. On SS, partial reversible formation of transition metal chlorides is also detected. Based on these findings, an artificial interface is engineered on Cu, significantly improving lithium plating/stripping efficiency. These insights contribute to solid-solid interface engineering strategies and advance the fundamental understanding of anode-free ASSLMBs.

1. Introduction

The anode-free cell configuration, which avoids the use of lithium metal during assembly, enables the highest possible energy density among all cell designs. The absence of lithium metal reduces raw material consumption, enhances manufacturing safety, and lowers production costs.[1] Additionally, incorporating a solid-state electrolyte (SSE) mitigates the safety risks associated with flammable liquid electrolytes, making this approach particularly promising for the development of practical anode-free batteries.

Sulfide-based SSEs, as one of the most promising candidates, can be readily deformed at room temperature, enabling efficient contact with the current collector through cold pressing.[2] This characteristic reduces material costs and simplifies the manufacturing process. The performance of anode-free solid-state batteries is largely governed by the interfacial properties of the current collectors, which influence lithium nucleation, plating/stripping efficiency, and cycling stability. Among the reported sulfide-based anode-free batteries, copper (Cu) and stainless steel (SS) are the most commonly used current collectors. The Cu current collector is commonly used in research because it functions as the anode-side current collector in commercial Li-ion batteries, owing to its excellent electrical and thermal conductivity as well as its cost-effectiveness. Several studies have reported the formation of Cu_2S on Cu current collectors when in contact with sulfide electrolytes.[3] The trace amounts of water can react with sulfide-based SSEs ($Li_{10}Si_{0.3}PS_{6.7}Cl_{1.8}$) to generate H_2S, which

Y. Wang, Y. Yuan, A. Ganesh, Y. Zhao
Department of Mechanical and Materials Engineering
University of Western Ontario
London, Ontario N6A 5B9, Canada
E-mail: yzhao628@uwo.ca

The ORCID identification number(s) for the author(s) of this article can be found under https://doi.org/10.1002/adma.202513090

DOI: 10.1002/adma.202513090

B. Jose, P. Kaghazchi
Institute of Energy Materials and Devices
Materials Synthesis and Processing (IMD-2)
Forschungszentrum Jülich GmbH, 52425 Jülich, Germany
E-mail: p.kaghazchi@fz-juelich.de

R. M. Faisal, L. Liu
Department of Chemistry
University of Western Ontario
London, Ontario N6A 5B7, Canada

K. H. Chan, J. Bekou
Flex-Ion Battery Innovation Center
Windsor, Ontario N8W 0A6, Canada

P. Kaghazchi
MESA+ Institute for Nanotechnology
University of Twente
P. O. Box 217, Enschede 7500AE, The Netherlands

subsequently reacts with Cu to form Cu_2S.[3b] However, under anhydrous conditions, sulfide-based SSEs remain virtually inert toward Cu.[3b] The SS current collector, on the other hand, shows lower reactivity toward the Li_6PS_5Cl compared with the Cu current collector, as evidenced by the cyclic voltammetry (CV) scan from 0 to 5 V versus Li/Li^+.[4] The surface roughness of SS has a significant influence on the efficiency and cycling stability of Li plating and stripping.[5] A moderately roughened SS surface increased the contact points between the SSE ($Li_{5.5}PS_{4.5}Cl_{1.5}$) and SS, thereby promoting uniform Li deposition and suppressing SSE decomposition.[5] Several studies have explored surface modification strategies, such as introducing the lithiophilic sites, to enhance interfacial stability and improve lithium plating/stripping efficiency on Cu and SS current collectors.[4,6]

Despite these advancements, the impact of naturally formed surface oxides on both Cu and SS current collectors was neglected in previous studies. For Cu foil, native oxide films spontaneously form on the surface upon exposure to air. These films are not self-passivating and can continue to grow through further oxidation at room temperature.[7] For the SS foil, the presence of Cr_2O_3 forms a passivation layer that prevents corrosion, effectively maintaining its stainless properties.[8] The thicknesses of these native oxide layers are always a few tens of nanometers. In theory, the native oxides on Cu and SS would significantly influence interfacial reactions, charge transfer resistance, and lithium nucleation behavior. Cu_2O, the main compound of the native oxide layer for Cu foil, undergoes a spontaneous conversion reaction with deposited Li to form a lithiophobic interface, which can negatively impact lithium deposition and interfacial stability.[9] On SS, during the electrodeposition of Li, the formation of metastable chromium-iron alloy nanoparticles was observed in the carbonate electrolyte.[10] However, for anode-free solid-state batteries, Cu and SS current collectors are frequently employed without explicitly mentioning pre-treatment procedures.[3,4,6d,11] While some studies have employed cleaning procedures with acetone and isopropyl alcohol and blow-dried with nitrogen gas[12] or sonicating the foils in ethanol,[6c,13] these organic solvents are insufficient for the complete removal of surface oxides. As a result, the presence and impact of spontaneously formed oxides on Cu and SS current collectors are often neglected in the analysis and interpretation of experimental findings. In solid-state anode-free batteries, the impact of the passivation layers of the current collectors remains unclear. Addressing this knowledge gap could provide valuable insights into interfacial engineering strategies, ultimately enhancing the long-term stability and efficiency of sulfide-based anode-free batteries.

In this study, we uncover a previously overlooked factor—the native oxide films on the current collector—and demonstrate their significant impact on interfacial chemistry and lithium deposition behavior in anode-free solid-state batteries. Different from the traditional perspective, the Cu current collector exhibits a more consistent Li plating and stripping performance than the SS current collector. In-operando and ex situ X-ray absorption spectroscopy (XAS), combined with DFT modelling, reveal that reactions between the sulfide SSE and native oxide layers on both Cu and SS current collectors occur even before electrochemical cycling. Prolonged cycling further leads to the formation of $CuSO_4$ and $Cr_2(SO_4)_3$. We further demonstrate that engineering a more favorable sulfide interface significantly enhances the Coulombic efficiency (CE) of lithium plating and stripping, compared to current collectors with native surface oxides or reduced oxide thickness. These findings advance the understanding of sulfide-based anode-free batteries and contribute to the optimization of interface design.

2. Results and Discussion

SS naturally develops a surface passivation layer, primarily composed of chromium oxide, which enhances its corrosion resistance and stability in various environments. Similarly, Cu forms a native oxide layer, typically consisting of Cu_2O and CuO, upon exposure to air. These passivation layers play a crucial role in influencing Li plating/stripping behavior. In this study, the surface composition of the commercialized 304 SS foil and the Cu foil was first investigated using time-of-flight secondary ion mass spectrometry (ToF-SIMS). Since Fe and Cr are the two elements with the highest weight percentage in 304 SS, their corresponding oxides were analyzed.[14] In **Figure 1a**, the FeO_2^- and Fe^- corresponding to FeO_x shortly decline after ≈20 s sputtering, while the CrO^-, CrO_2^-, and CrO_3^-signals that represent Cr_2O_3 attenuate after ≈40 s sputtering. According to the 3D reconstructed surface image in Figure 1b,c, both FeO_x and Cr_2O_3 distribute uniformly on the surface. The depth profile of the Cu foil is presented in Figure 1d. The CuO_2^- signal that corresponds to the native CuO_x present on the surface, which shortly decreases after 16 s sputtering, while the Cu^- signal peaks at ≈30 s and plateaus afterwards. The 3D reconstructed surface image in Figure 1e,f also demonstrates the presence of homogeneous CuO_x on the surface of the Cu foil. The surface composition of both foils was further understood by X-ray photoelectron spectroscopy (XPS). As shown in Figure 1g, the peaks at 706.8, 709.5, 711.2, and 713.2 eV in the Fe $2p_{3/2}$ XPS spectrum correspond to Fe metal, Fe^{2+} (oxide), Fe^{3+} (oxide), and Fe^{3+} (hydroxide), respectively.[14] The peaks at 574.1, and 576.4 eV in the Cr $2p_{3/2}$ spectrum are assigned to Cr metal and Cr^{3+} (oxide), respectively (Figure 1h).[14] The small peak on the low binding energy side of the envelope was assigned to a defect-derived satellite, which likely originates from near-surface point defects or dislocations associated with local mechanical strain in the structure, as has been previously reported.[15] The corresponding O 1s spectra are shown in Figure S1 (Supporting Information), where the peaks at 529.7 and 531.7 eV are attributed to metal oxide and metal hydroxide species, respectively, present on the SS surface.[14] Figure 1i shows the Cu $2p_{3/2}$ spectrum for the Cu foil. The deconvolution reveals the presence of Cu/Cu_2O, CuO, and $Cu(OH)_2$ at 932.5, 934, and 935.2 eV, respectively.[16] The peaks of Cu and Cu_2O are indistinguishable due to their similar Cu $2p_{3/2}$ binding energy.[16,17] The surface morphology of the SS foil and the Cu foil was characterized by SEM. The SS foil has a smooth surface with small pits found on the surface (Figure 1j), while the surface of Cu foil is rougher (Figure 1k). Passivation layers naturally form on SS and Cu current collectors, yet their influence on electrolyte–current collector interfacial reactions in anode-free cells is often overlooked.

The plating and stripping behaviour of Li on commercialized SS and Cu was evaluated using Li metal counter electrode and Li_6PS_5Cl SSE. **Figure 2a,b** depict the typical voltage profile of Li-SS and Li-Cu cells tested at 0.1 mA cm^{-2} and 0.5 mAh cm^{-2}, with a stripping voltage cut-off at 1 V versus Li/Li^+. The

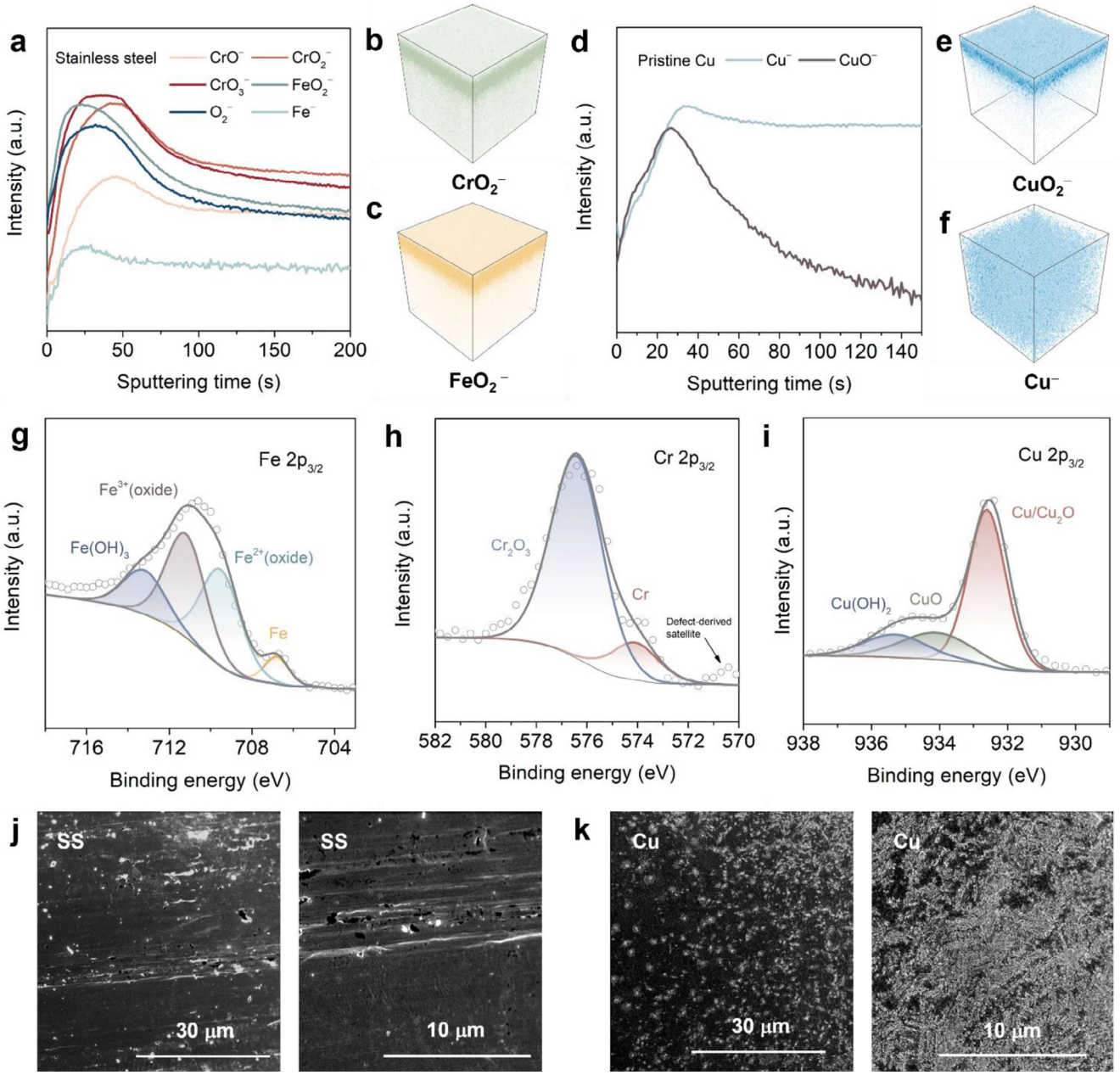

Figure 1. a) The ToF-SIMS depth profile of 304 SS foil. The ToF-SIMS 3D rendering images of b) CrO_2^- and c) FeO_2^- on 304 SS foil. d) The ToF-SIMS depth profile of Cu foil. The ToF-SIMS 3D rendering images of e) CuO_2^- and f) Cu^- on Cu foil. g) The Fe $2p_{3/2}$ XPS spectrum of 304 SS foil. h) The Cr $2p_{3/2}$ XPS spectrum of 304 SS foil. i) The Cu $2p_{3/2}$ XPS spectrum of Cu foil. The SEM image of j) pristine 304 SS foil surface and k) pristine Cu foil surface.

electrochemical performance of Li–SS and Li–Cu cells was also tested at current densities of 0.2 and 0.5 mA cm^{-2}, which resulted in unstable cycling (Figure S2, Supporting Information). Since the objective of this study is to elucidate the interfacial reactions between Li_6PS_5Cl and the surface passivation layers of SS and Cu at different stages of Li plating/stripping, a lower current density of 0.1 mA cm^{-2} was employed to ensure prolonged cycling stability. The Li-SS cell delivers an initial CE of 82.2%, while the Li-Cu cell exhibits a slightly higher initial CE of 87.7% (Figure 2c,d). The irreversible capacities for both SS and Cu current collectors are possibly caused by the consumption of Li during the interphase formation at the first cycle. At the 10th cycle, notably unstable Li stripping behaviour was observed from 0.1 V versus Li/Li^+ on SS, while signs of interfacial degradation do not appear until 0.5 V versus Li/Li^+ on Cu. To probe the degradation process of the interface, the effect of different voltage cut-offs on the Li plating and stripping efficiency on the two current collectors was further explored. In Figure 2c,d, the plating and stripping efficiency of Li on SS and Cu with varied stripping voltage cut-offs at 0.1, 0.2, 0.5, and 1 V were compared. Incomplete stripping of Li at

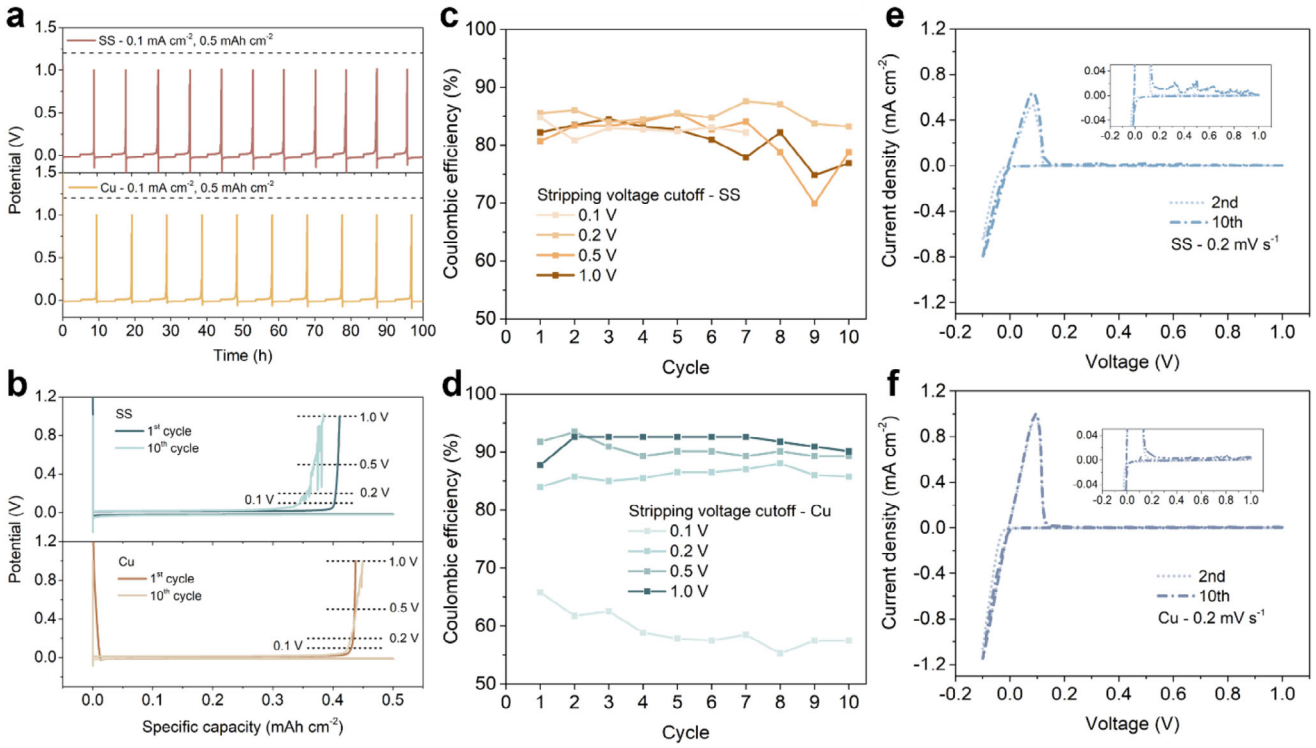

Figure 2. a) Voltage profile of Li-SS cell tested at 0.1 mA cm^{-2} and 0.5 mAh cm^{-2}, with a stripping voltage cut-off at 1 V versus Li/Li^+ (top); voltage profile of Li-Cu cell tested at 0.1 mA cm^{-2} and 0.5 mAh cm^{-2}, with a stripping voltage cut-off at 1 V versus Li/Li^+ (bottom). b) First- and tenth-cycle plating/stripping voltage profile of Li-SS cell (top); first- and tenth-cycle plating/stripping voltage profile of Li-Cu cell (bottom). c) CE of Li-SS cells with stripping voltage cut-off at 0.1, 0.2, 0.5, and 1 V. d) CE of Li-Cu cells with stripping voltage cut-off at 0.1, 0.2, 0.5, and 1 V. e) Second- and tenth-cycle CV of Li-SS cell at a scan rate of 0.2 mV s^{-1}. f) Second- and tenth-cycle CV of Li-Cu cell at a scan rate of 0.2 mV s^{-1}.

low stripping voltage cut-off and degradation of the SSE-current collector interface at high stripping voltage cut-off both negatively affect the resulting CE. The CE obtained on SS at different voltage cut-offs is scattered within 69.9-87.5% and does not present a discernible trend. The voltage profile of the 10th cycle at each voltage cut-off is included in Figure S3 (Supporting Information). The Li-SS cell with a stripping voltage cut-off set at 0.1 V could only last for 7 cycles and then short afterwards, possibly due to the build-up of unstripped Li on SS and the growth of Li dendrites. Even with a low voltage cut-off of 0.2 V, severe interface degradation was seen at the 10th cycle (Figure S3, Supporting Information), indicating that the SS current collector could hardly accommodate the deep discharge in an anode-free full cell. Unlike the scattered CE obtained on SS, the CE across the first 10 cycles on Cu is relatively stable. At a stripping voltage cut-off of 1 V, the Li plating and stripping efficiency on Cu is notably higher compared with that on SS, likely due to the deferred interfacial degradation in the high voltage region (Figure 2b). The first 10-cycle CE decreases with descending stripping voltage-cutoff, and no notable sign of interfacial degradation was observed before 0.5 V (Figure S4, Supporting Information), showing that the obtained CE was mainly dominated by the Li stripping process without major interference of the side reactions and interfacial degradation mainly happened in the high voltage region (>0.5 V). The CV was conducted at a scan rate of 0.2 mV s^{-1} to investigate the Li plating/stripping on SS and Cu. At the second cycle, the SS resulted in a relatively low Li plating/stripping peak current density of 0.53 and 0.65 mA cm^{-2}, respectively (Figure 2e). The peak current density increases over the cycle, suggesting that the interfacial reactions change over cycles, which promotes the reaction kinetics of the Li plating/stripping process. In contrast, Cu enabled a much higher Li plating/stripping peak current density of 0.97 and −1.06 mA cm^{-2} at the second cycle, likely attributed to the less resistive interface on the Cu current collector (Figure 2f).[18] At the tenth cycle, the current response beyond 0.2 V versus Li/Li^+ is significantly higher on SS compared to Cu, indicating a more severe side reaction on the SS current collector. This observation is consistent with the findings from previous galvanostatic testing.

The distinct interphases formed on Cu and SS result in different lithium plating and stripping behaviors: the Cu interphase enhances Li plating/stripping efficiency and maintains greater stability at high stripping voltages. To examine the interphase composition and its impact on electrochemical performance, in situ synchrotron-based X-ray absorption near-edge structure (XANES) spectroscopy was used to analyze changes in the local chemical environments of elements in the system. The experimental setup is illustrated in **Figure 3**a. The in situ cell was placed on the sample holder under a vacuum of 10^{-7} torr to optimize flux for edges with lower energies. The Cu and SS mesh current collectors were utilized to enable the investigation of interphase evolution during Li plating and stripping. The detailed in situ cell configuration is illustrated in Figure S5 (Supporting Information). The P K-edge, S K-edge and Cl K-edge spectra were collected using the fluorescence yield (FLY) mode at specific

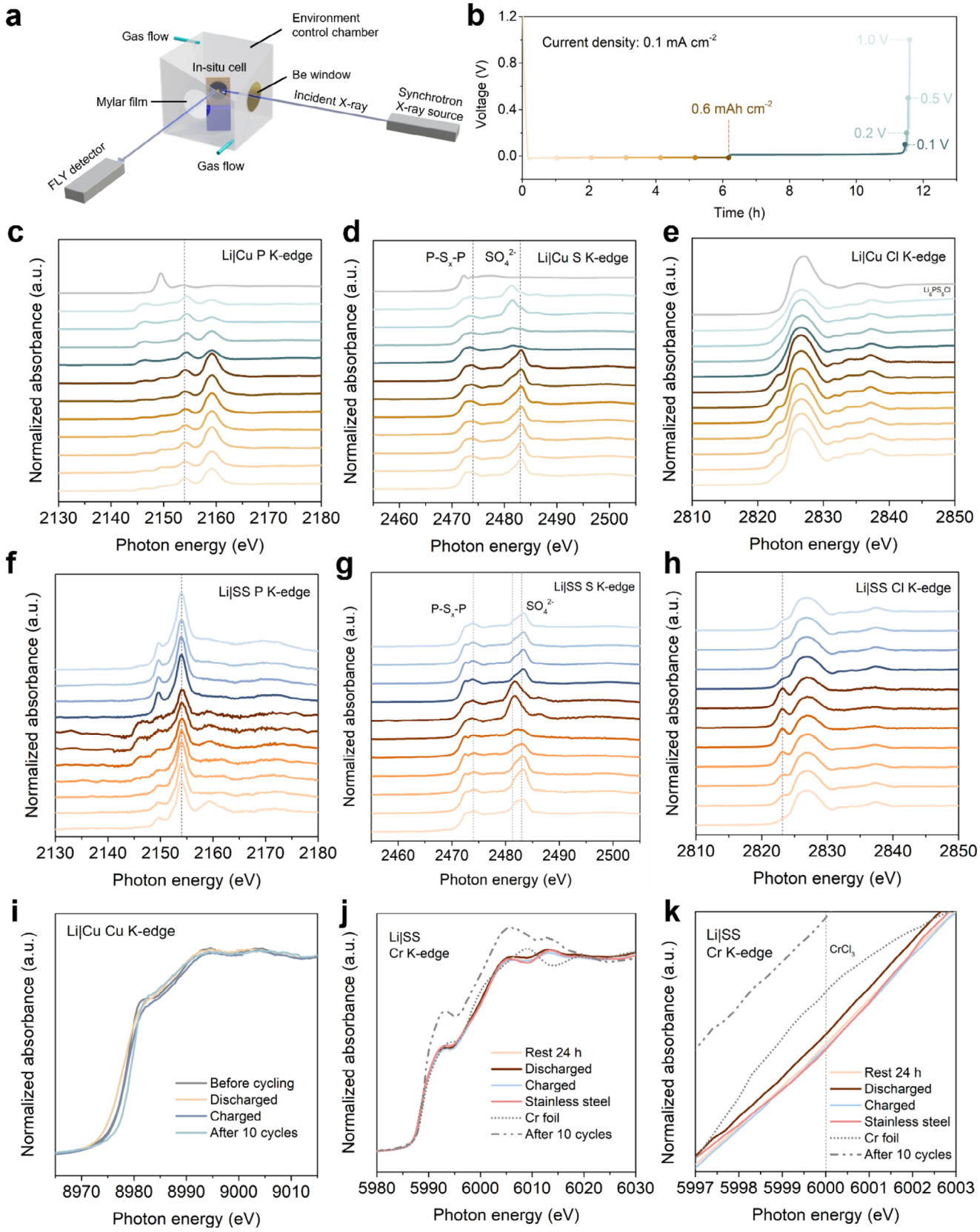

plating capacities and stripping voltage cut-offs for both the Li|Cu and Li|SS systems (Figure 3b). The P K-edge, S K-edge, and Cl K-edge spectra for Li_6PS_5Cl were also included for reference. These spectra show good agreement with literature-reported data[19] and further demonstrate that the Kapton tape effectively isolates the sample from the ambient environment, providing sufficient oxygen barrier properties. All P K-edge measurements were calibrated against the first derivative maximum of tricalcium phosphate ($Ca_3(PO_4)_2$) at 2152.7 eV.[20] The white line at 2149.55 eV corresponds to the electron transition from 1s orbitals to the unoccupied electronic state of 3p character,[21] which represents the PS_4^{3-} in pristine Li_6PS_5Cl structure (Figure 3c).[19] Upon contact with the Cu current collector, the PS_4^{3-} feature diminished, further weakening during lithium stripping and eventually disappearing completely (Figure 3c). The peaks at 2154 eV were assigned to the formation of P-S_x-P/PO_4^{3-}.[19,22] The P-S_x-P/PO_4^{3-} formed upon contact with the Cu current collectors and remained on the current collectors throughout the plating and stripping process. The identification of P-S_x-P is supported by the peak at ≈2474 eV in the S K-edge spectra (Figure 3d), which can be detected on Cu before cycling.[19] No significant change in the P-S_x-P feature on S K-edge spectra is observed on Cu throughout cycling. For pristine Li_6PS_5Cl, the intense peak at 2472.3 eV can be attributed to the S 1s orbital to unoccupied states of S 3p character. The notable peak at 2483 eV may be attributed to the formation of SO_4^{2-},[19] which is likely a result of $CuSO_4$ formation.[23] Since the cell assembly was conducted in an Ar-protected environment, the only source of oxygen is the surface passivation layer on the current collector. This indicates that the reaction occurred between the SSE and the surface oxide passivation layer. The SO_4^{2-} feature can be detected throughout the Li plating cycle. During Li stripping, the SO_4^{2-} feature at 2483 eV attenuated while another peak at 2481.5 eV emerges, which can be possibly assigned to the detection of Li_2SO_4 formation.[24] The Cl K-edge is shown in Figure 3e. For the Li|Cu cell, the pre-edge peak observed at ≈2822.9 eV may be attributed to the formation of metal-induced gap states (MIGS), which have been previously reported at LiCl/Cu interfaces.[25] These states arise due to the proximity to the metal rather than any local modification of chemical bonds.[25] Raman spectroscopy was also employed to analyze the interfacial chemistry of the Cu current collector (Figure S6, Supporting Information). The peak at ≈425 cm^{-1} corresponds to the PS_4^{3-} unit in Li_6PS_5Cl. Two samples were examined: (i) Li plated on Cu (1 mAh cm^{-2}) and (ii) after Li was fully stripped to a cut-off voltage of 1 V. In both cases, a peak at ≈417 cm^{-1} was observed, indicating local distortion of the PS_4^{3-} tetrahedral induced by oxygen incorporation.[26]

On the SS current collector, the PS_4^{3-} feature weakened during Li plating but re-formed during Li stripping, as shown on the P K-edge spectra (Figure 3f). The P-S_x-P/PO_4^{3-} formed upon contact with SS and remains on the SS throughout the Li plating and stripping process. From S K-edge spectra (Figure 3g), the intensity of P-S_x-P increases during Li plating and diminishes during stripping, aligning with the variations in the PS_4^{3-} feature seen in the P K-edge spectra. The SO_4^{2-} formation at 2483 eV was also observed on the SS before cycling. A peak potentially associated with Li_2SO_4 formation emerges after 0.5 mAh cm^{-2} of Li plating. During the Li stripping, the SO_4^{2-} feature reverted back to 2483 eV, suggesting the reversible formation of the sulfate species. From the Cl K-edge spectra in Figure 3h, a much more prominent pre-edge peak at ≈2823.2 eV emerged during the Li plating on SS. This pre-edge feature is attributed to the increase in covalency resulting from the mixing of Cl 3p orbitals and metal d-orbitals.[27] Similar features were reported in Cl K-edge spectra of Fe-Ni and Fe-Cr alloys exposed in the Cl-rich environment.[28] The intensity of the pre-edge peak attenuated during the stripping process, indicating that the formation of the transition metal chloride is reversible.

The normalized Cu K-edge spectra of the Cu mesh current collector obtained from the in situ experiment and the Cu foil after 10-cycle Li plating and stripping are presented in Figure 3i. The edge position shifted to the lower energy after the first-cycle plating, likely due to an increased Cu_2S content on the interface, as the higher covalency of Cu—S bonds compared to Cu—O bonds results in a lower edge energy.[29] The edge position reverts back after the stripping process. After 10-cycle plating/stripping, the absorption edge shifts to higher energy compared to the pristine state, possibly due to the increased $CuSO_4$ content.[30] Although Fe is the most abundant element in 304 SS, no noticeable peak shift was observed in the Fe K-edge spectra during the Li plating and stripping process. This suggests that either Fe has minimal involvement in interfacial reactions or any changes in Fe were obscured by the bulk signal (Figure S7, Supporting Information). Negligible differences were also observed in the Ni K-edge spectra after cycling, indicating minimal alteration in the Ni environment during the process (Figure S8, Supporting Information). The Cr K-edge spectra were recorded to analyze the chemical changes on SS current collectors at four stages: before cycling, after the first discharge, after the first charge, and after 10 plating/stripping cycles (Figure 3j). During Li plating, an edge feature appeared at ≈6000 eV, which has been previously characterized as $CrCl_3$ (Figure 3k).[31] After 10 plating/stripping cycles, the enhanced peak feature at ≈6006 eV may be attributed to the increased $Cr_2(SO_4)_3$ at the interface.[32] These findings demonstrate that Li_6PS_5Cl undergoes chemical degradation upon contact with Cu and SS surfaces even before electrochemical cycling, influencing subsequent interfacial reactions. The Cu K-edge analysis reveals the formation of Cu_2S and $CuSO_4$ over multiple plating/stripping cycles, while SS current collectors exhibit minimal Fe and Ni involvement in interfacial reactions. However, Cr undergoes notable changes, with the probable formation of $CrCl_3$ and $Cr_2(SO_4)_3$ over cycling. Raman spectroscopy was

Figure 3. In situ and ex situ XAS measurements. a) Schematic illustration of the in situ synchrotron-based XANES study setup of Cu and SS current collectors. b) Voltage profile of a typical Li plating/stripping process with marked specific capacity and voltage at which the XAS spectra were conducted. The c) P K-edge, d) S K-edge, and e) Cl K-edge acquired from the Cu mesh current collector. The f) P K-edge, g) S K-edge, and h) Cl K-edge acquired from the SS mesh current collector. i) The Cu K-edge XAS spectra acquired from the Cu mesh current collector during the in situ experiment at different stages (before cycling, discharged, and charged) and the Cu foil current collector disassembled after 10 Li plating/stripping cycles. j) The Cr K-edge XAS spectra acquired from pristine SS foil, Cr metal foil, and SS foil current collector disassembled after resting for 24 h, first discharge, first charge, and 10 plating/stripping cycles. k) A magnified view of the Cr K-edge graph.

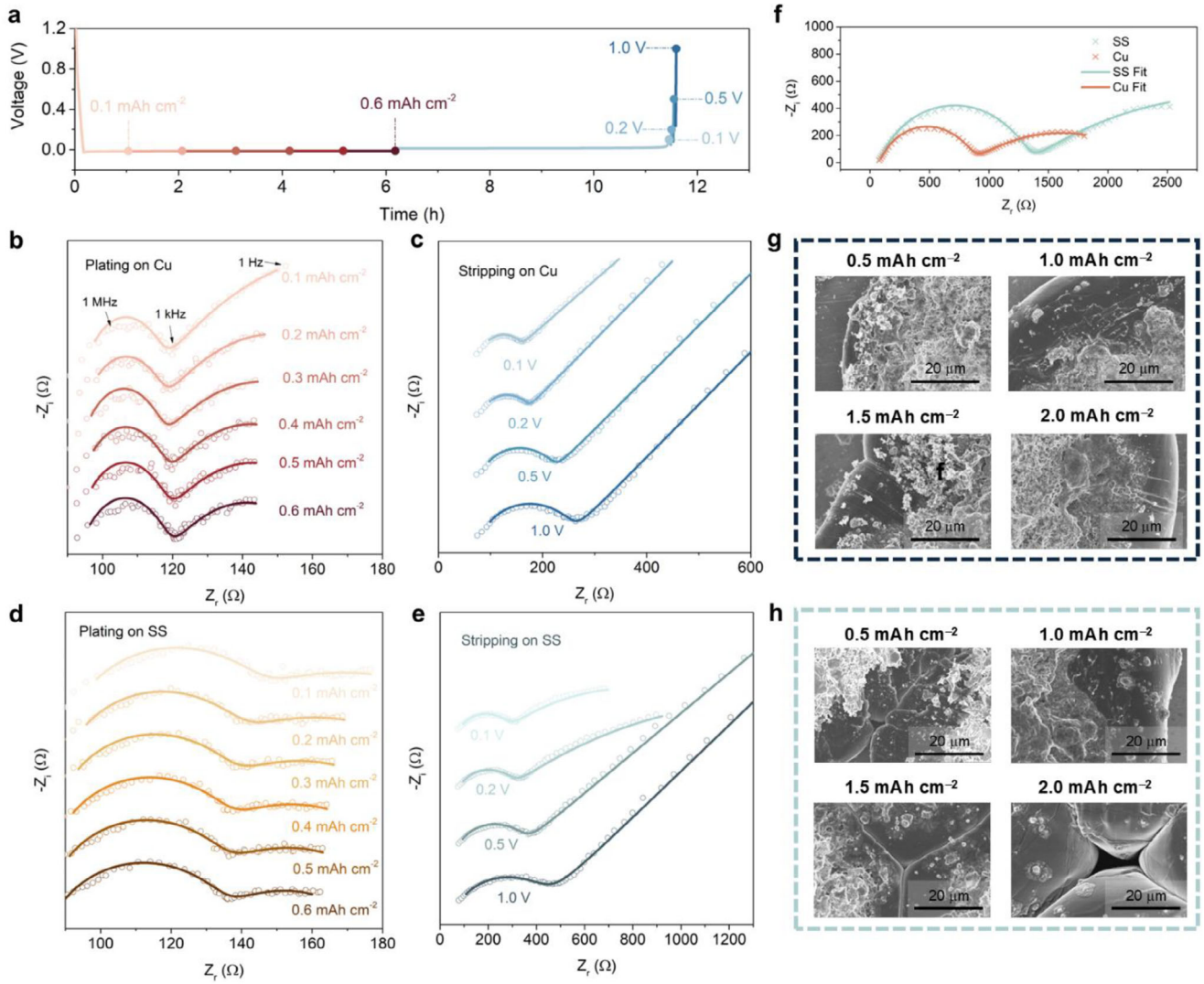

Figure 4. a) Voltage profile of a typical Li plating/stripping process with marked specific capacity and voltage, at which the in-operando EIS measurements were conducted. The EIS Nyquist plots of b) Li plating and c) stripping on Cu current collectors in the first cycle. The EIS Nyquist plots of d) Li plating and e) stripping on SS current collectors in the first cycle. f) The comparison of EIS Nyquist plots of Li|Cu and Li|SS after 10-cycle plating/stripping. g) The SEM images of 0.5, 1.0, 1.5, and 2.0 mAh cm^{-2} of Li deposits on Cu. h) The SEM images of 0.5, 1.0, 1.5, and 2.0 mAh cm^{-2} of Li deposits on SS.

further employed to investigate the interfacial chemistry of the SS current collector (Figure S9, Supporting Information). Two conditions were examined: (i) Li plated on SS (1 mAh cm^{-2}) and (ii) after Li was fully stripped to a cut-off voltage of 1 V. As with Cu current collectors, a peak at ≈417 cm^{-1} was observed, indicating local distortion of the PS_4^{3-} tetrahedral induced by oxygen incorporation.[26] These results emphasize the pivotal role of the current collector's surface passivation layer in interphase evolution, highlighting its interaction with the sulfide solid-state electrolyte in affecting electrochemical performance.

The in situ electrochemical impedance spectroscopy (EIS) was conducted to investigate the evolution of the interfacial properties during the Li plating/stripping. The EIS spectra were collected after 0.1, 0.2, 0.3, 0.4, 0.5, and 0.6 mAh cm^{-2} of Li deposited on the current collectors, respectively. In the subsequent stripping cycle, the EIS measurements were carried out at voltage cut-offs of 0.1, 0.2, 0.5, and 1.0 V, as shown in **Figure** 4a. Based on the XAS analysis, the interphase starts to establish when the current collector comes into contact with the sulfide SSE, which is further supported by the EIS spectra measured during the resting step before the electrodeposition starts (Figure S10, Supporting Information). In Figure 4b, the high-frequency loop was attributed to the charge transfer (CPE_{SEI}) and the charge transfer resistance (R_{SEI}) of the interface formed on the Cu, while the low-frequency loop was assigned to the charge transfer of plated Li (CPE_{Li}) and the charge transfer resistance of Li/Li^+ (R_{Li}).[33] The large resistance of the assembled cell was largely reduced after the Li nucleated onto the current collector.[12] The interfacial charge transfer resistance gradually increases during the stripping process (Figure 4c). The fitting parameters obtained from the time-resolved EIS of the Cu|Li_6PS_5Cl|Li cell are presented in Table S1 (Supporting Information). The interphase formed on

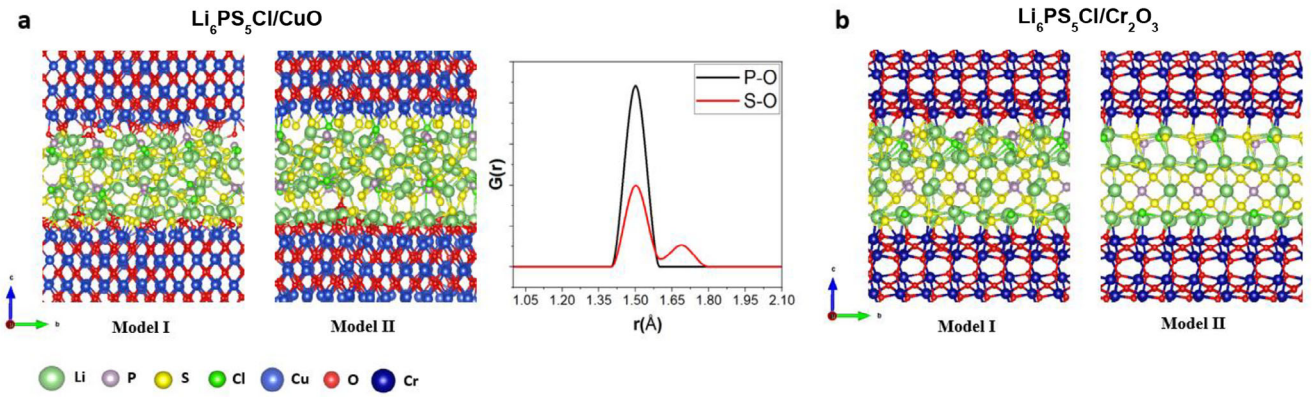

Figure 5. Computed atomistic structures of a) Li_6PS_5Cl/CuO and b) Li_6PS_5Cl/Cr_2O_3 interfaces with two different terminations, obtained through electrostatic analysis and DFT calculations. Radial distribution function for P—O and S—O bonds in Li_6PS_5Cl/CuO interface is also presented in a).

SS exhibits a higher charge transfer resistance (R_{SEI}) than that on Cu during both the plating and stripping processes (Figure 4d,e). The fitting parameters obtained from the time-resolved EIS of the SS|Li_6PS_5Cl|Li cell are presented in Table S2 (Supporting Information). After 10-cycle plating/stripping, the interphase formed on Cu still exhibited a lower interfacial resistance than that formed on SS (768 Ω versus 1252 Ω), suggesting the interphase of lower charge transfer resistance formed on Cu facilitates the Li plating/stripping throughout cycling (Figure 4f). The fitting parameters for both cells after 10 cycles are presented in Table S3 (Supporting Information). The interphase formed prior to electrochemical cycling plays a critical role in governing Li nucleation behavior on different current collectors. Specifically, Cu exhibits a nucleation overpotential of −0.0162 V, whereas SS shows a slightly higher value of −0.0267 V, indicating that the energy barrier between nucleation and growth is smaller on Cu, which favors a more uniform Li deposition compared to SS (Figure S11, Supporting Information). The variation in interfacial charge transfer resistance of the interphase results in distinct lithium deposition morphologies at different stages, as observed through scanning electron microscopy (SEM). On Cu, Li deposits tend to form a single, integrated large structure (Figure 4g), whereas on SS, the deposits are smaller in size and exhibit a porous morphology at higher capacity (Figure 4h). The lower-magnification images of the 2 mAh cm^{-2} Li deposit on Cu and SS are presented in Figure S12 (Supporting Information), providing an overview of the overall morphology and spatial distribution of the Li deposit. The Li deposition on SS became more uneven and tortuous at higher current densities (0.2 and 0.5 mA cm^{-2}), compared to the relatively smoother morphology on the Cu current collector (Figure S13, Supporting Information). The porous Li deposit observed on SS potentially promotes the growth of dendrites and hinders long-term cycling stability.

To further understand the degradation mechanism of sulfide electrolyte on current collectors, first-principles calculations based on density functional theory (DFT) were performed on the CuO(001)/Li_6PS_5Cl(001) and Cr_2O_3(001)/Li_6PS_5Cl(001) interfaces. We have applied an extensive Coulomb energy calculation to identify the minimum energy configurations at the electrolyte/current collector interfaces, followed by DFT optimization (a detailed description of the computational methodology can be found in the Supporting Information). The results from the Li_6PS_5Cl/CuO interface (**Figure 5a**) show that the stability of the electrolyte is significantly influenced by the presence of CuO. Strong interactions between the components have been observed, including bond formations between Cu and S, Cu and P, P and O, S and O, Li and S, Li and O, as well as Li and Cl. Radial distribution function for Li_6PS_5Cl/CuO interface shows formation of P—O and S—O bonds (Figure 5a), whose bond lengths are consistent with those of experimentally measured in PO_4^{3-} (P—O bondlength of ≈1.5 Å[34]) and SO_4^{2-} (S—O bondlength of ≈1.49 Å[35]), indicating the probability of formation of phosphate (PO_4^{3-}) and sulfate (SO_4^{2-}) species at the interface, namely $CuSO_4$ and Li_2SO_4. Our DFT calculation on the Li_6PS_5Cl/Cr_2O_3 interface (Figure 5b), however, indicates a higher stability of Cr_2O_3 compared to CuO in contact with Li_6PS_5Cl, which can be clearly seen from the corresponding optimized atomistic structure. The interfacial interactions for the former case suggest a potential for the formation of Cr—S, Cr—Cl, Li—Cl, and Li—O bonds. The Cr—S bond can be seen as the initial stage of formation of chromium sulfate species such as $Cr_2(SO_4)_3$, while Cr—Cl bond formation, which could be considered as an initial stage of formation of $CrCl_3$. Phosphate and sulfate species were observed (Figure 3) to form at both the current collector interfaces, attributed to reactions between the sulfide electrolyte and surface oxides.

Since the surface oxides are the sole source of oxygen, they contribute to the irreversible formation of SO_4^{2-} and PO_4^{3-}, thereby affecting the CE of lithium plating/stripping. To further investigate the impact of the oxide layer on Li plating/stripping CE, the Cu foil was pretreated with acetic acid to reduce the surface oxide content and subsequently used to evaluate the Li plating/stripping behaviour.[36] The top-view SEM image of the acetic acid-treated Cu is shown in Figure S14 (Supporting Information). From the ToF-SIMS depth profile in **Figure 6a**, the intensity of Cu^- and CuO^- reaches the maximum at ≈15 s, showing that the thickness of copper oxide has been significantly reduced. The corresponding 3D rendering images of Cu^- and CuO^- are presented in Figure 6b,c. The Li plating/stripping CE on acetic-treated Cu was similar to that on pristine Cu, as shown in Figure 6g, likely due to the incomplete removal of surface oxide. This interpretation is further supported by the Cu $2p_{3/2}$ and Cu $L_3M_{4,5}M_{4,5}$

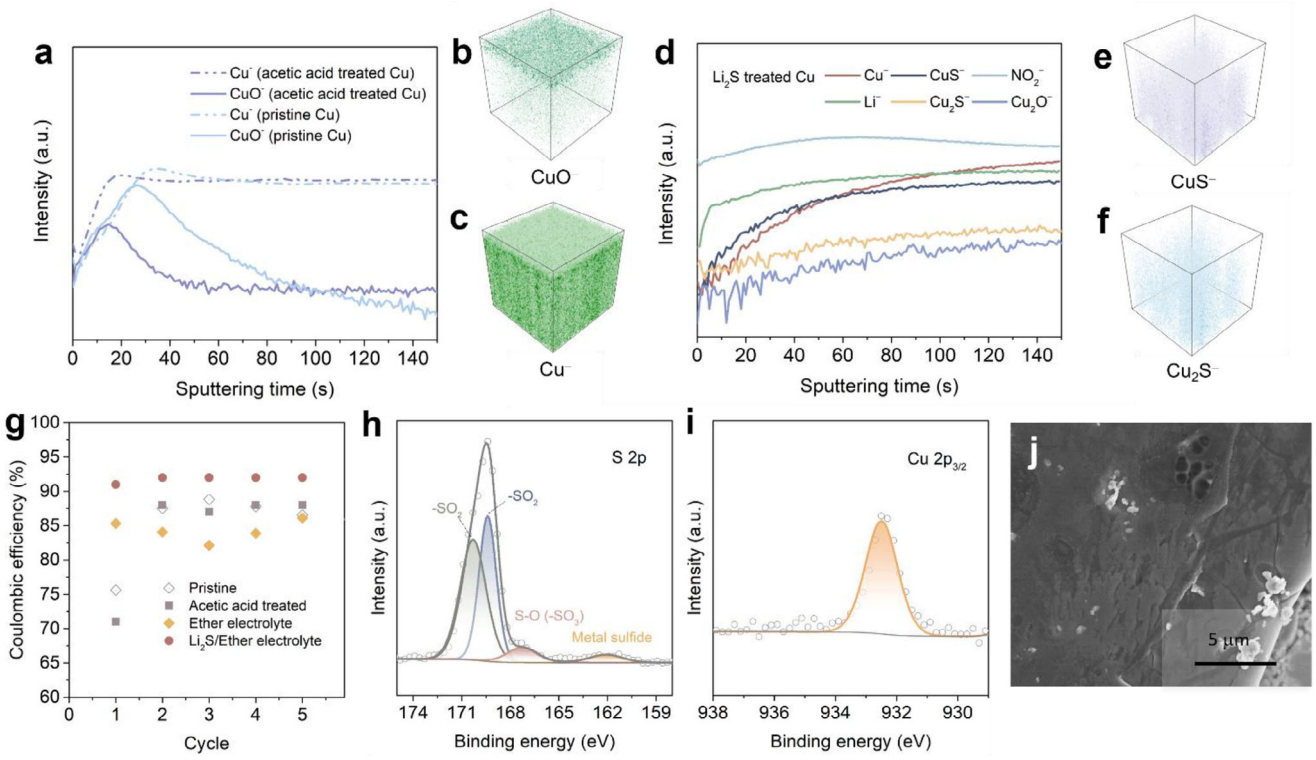

Figure 6. a) The ToF-SIMS depth profile of pristine Cu foil and acetic acid-treated Cu foil. The ToF-SIMS 3D rendering images of b) CuO^- and c) Cu^- on acetic acid-treated Cu foil. d) The ToF-SIMS depth profile of Li_2S-treated Cu foil. The ToF-SIMS 3D rendering images of e) CuS^- and f) Cu_2S^- on Li_2S-treated Cu foil. g) Li plating/stripping CE on pristine-, acetic acid treated-, ether-based electrolyte treated-, and Li_2S treated Cu conducted at 0.1 mA cm^{-2} and 0.2 mAh cm^{-2}, with stripping voltage cut-off at 0.5 V versus Li/Li^+. h) The S 2p spectrum of Li_2S treated Cu foil. i) The Cu $2p_{3/2}$ spectrum of Li_2S treated Cu foil. j) The SEM image of 0.2 mAh cm^{-2} Li deposited on Li_2S treated Cu foil at 0.1 mA cm^{-2}.

Auger spectra. In the Cu $2p_{3/2}$ spectrum (Figure S15, Supporting Information), the peak at ≈932.5 eV is attributed to Cu_2O on the acetic-treated Cu surface,[16] and consistently, the peak at ≈916.99 eV in the Cu $L_3M_{4,5}M_{4,5}$ Auger spectrum (Figure S16, Supporting Information) is also assigned to Cu_2O.[37]

As a strategy to stabilize the Cu current collector interface, the native surface oxide was converted to sulfide through S^{2-} treatment, thereby suppressing the formation of SO_4^{2-}- and PO_4^{3-}-containing species. In addition, Li_2O[38] and LiF[39] generated in situ by soaking Cu in ether-based electrolyte[40] were utilized to enhance Li plating/stripping reversibility. To integrate these effects, Cu was treated with Li_2S-saturated ether electrolyte, with the clear supernatant employed to achieve controlled surface modification. The Li_2S-treated Cu interface was first characterized using ToF-SIMS. The depth profiles of Li^-, Cu_2O^-, CuS^-, and Cu_2S^- suggest the coexistence of Cu_2O and Cu_2S on the Cu surface and further reveal that the Li-containing sulfide-based interphase formed is substantially thicker than the native oxide layer and primarily composed of sulfide species. (Figure 6a,d–f). This Li_2Streated Cu interface facilitates a high initial and sustained plating/stripping CE (>90%), surpassing that of pristine Cu and acetic acid-treated Cu (Figure 6g). The Li plating/stripping CE on Cu treated with the ether electrolyte alone is also shown, exhibiting a lower CE compared to that on pristine Cu. The corresponding top-view SEM images of ether-treated Cu are presented in Figure S17 (Supporting Information). The effectiveness of the Li_2S treatment was demonstrated using three repeated cells (Figure S18a, Supporting Information), and the typical Li plating and stripping voltage profiles are included in Figure S18b. The CE of the $Li|Li_6PS_5Cl|Li_2S$ treated Cu half cell over cycling is shown in Figure S19 (Supporting Information). Although the CE remains high (≥90%) in the first 5 cycles, it becomes scattered after approximately eight cycles. This observation suggests that the sulfide interface facilitates improved initial plating/stripping behavior relative to the native oxide interface. To improve the long-term stability and practical applicability, further optimization is necessary, with emphasis on tailoring the chemical composition of the sulfide interface and developing three-dimensional architectures to better accommodate the volume changes associated with repeated plating/stripping. The surface composition of Li_2S-treated Cu was further analyzed using XPS. In S 2p spectra (Figure 6h), peaks at 169.3 and 170.2 eV are the characteristic peaks of sulfone (—SO_2) from LiTFSI salt.[41] The peak at 167.2 eV can be assigned to LiTFSI decomposition species formed.[42] The peak at 162.1 eV can be assigned to either Li_2S or Cu_2S.[43] The treated surface does not contain $Cu(OH)_2$ or CuO (Figure 6i), due to the absence of the satellite feature related to the d^9 configuration in the ground state of Cu (Figure S20, Supporting Information).[17b,44] The similar Cu 2p binding energies of Cu, Cu_2O, and Cu_2S make it challenging to distinguish these species in the Cu 2p XPS spectrum (Figure 6i).[45] Ex situ XANES was conducted to investigate the interfacial chemistry of the

Li_2S-treated Cu (Figure S21, Supporting Information). After the treatment, the edge position shifts to lower energy, which can be attributed to the increased presence of Cu_2S at the interface. This shift arises because Cu—S bonds are more covalent than Cu—O bonds, leading to a reduced edge energy.[29] The SEM image of 0.2 mAh cm^{-2} Li deposited on Li_2S treated Cu foil at 0.1 mA cm^{-2} is shown in Figure 6j, demonstrating the smooth and dense Li deposits achieved on the modified Cu foil. The same surface treatments (acetic acid and Li_2S) were applied to SS; however, these resulted in the formation of an unstable interface, which in turn led to poor CE (Figure S22, Supporting Information).

3. Conclusion

This study first highlights the neglected role of the native oxide films of the current collector in interfacial chemistry and lithium deposition behavior for anode-free solid-state batteries. Although Cu is generally considered an unstable current collector for sulfide-based SSEs, it demonstrates more stable Li plating/stripping behavior compared to SS. In-operando XAS and DFT computational modelling identified P-S_x-P/PO_4^{3-} and SO_4^{2-} species at both interfaces even before electrochemical cycling, suggesting the chemical interactions between the sulfide SSE and surface oxides. Furthermore, the partial reversible formation of transition metal chlorides on SS was observed during cycling. The change in Cu K-edge of Cu and Cr K-edge of SS after 10-cycle Li plating/stripping may be attributed to the formation of $CuSO_4$ and $Cr_2(SO_4)_3$. To improve the Li plating/stripping CE, the removal of surface oxides was initially attempted, followed by the construction of a sulfide interface. This study promotes the understanding of solid-solid interfaces in anode-free ASSLMBs and provides critical design strategies to improve interfacial stability and overall battery performance.

Supporting Information

Supporting Information is available from the Wiley Online Library or from the author.

Acknowledgements

Y.W. and B.J. contributed equally to this work. The authors thank the support from the Natural Science of Engineering Research Council of Canada (NSERC), the Canada Foundation for Innovation (CFI), Mitacs, Flex-Ion Battery Innovation Center, and the University of Western Ontario. The synchrotron research was conducted at the Soft X-ray Microcharacterization Beamline (SXRMB) of the Canadian Light Source (CLS), which is supported by the Canada Foundation for Innovation (CFI), the Natural Sciences and Engineering Research Council (NSERC), the National Research Council (NRC), the Canadian Institutes of Health Research (CIHR), the Government of Saskatchewan, the University of Saskatchewan. The authors also gratefully acknowledge the great help from Dr. Mohsen Shakouri and Dr. Qunfeng Xiao at the SXRMB. The EasyXAFS300+ was co-funded by the Canadian Foundation for Innovation (John R. Evans Leaders Fund), and the Ontario Research Fund (Small Infrastructure Fund). The authors would like to thank Javier Diaz and Justin Zheng for their assistance with battery assembly. Computation time granted through JARA HPC on the supercomputer JURECA[46] at Forschungszentrum Jülich under Grant No. jiek12 is gratefully acknowledged by the authors.

Conflict of Interest

The authors declare no conflict of interest.

Data Availability Statement

The data that support the findings of this study are available from the corresponding author upon reasonable request.

Keywords

anode-free solid-state batteries, current collectors, DFT modelling, In-situ X-ray absorption spectroscopy, passivation layers

Received: July 8, 2025
Revised: August 23, 2025
Published online: September 7, 2025

[1] C. Heubner, S. Maletti, H. Auer, J. Hüttl, K. Voigt, O. Lohrberg, K. Nikolowski, M. Partsch, A. Michaelis, *Adv. Funct. Mater.* **2021**, *31*, 2106608.
[2] S. E. Sandoval, C. G. Haslam, B. S. Vishnugopi, D. W. Liao, J. S. Yoon, S. H. Park, Y. Wang, D. Mitlin, K. B. Hatzell, D. J. Siegel, P. P. Mukherjee, N. P. Dasgupta, J. Sakamoto, M. T. McDowell, *Nat. Mater.* **2025**, *24*, 321.
[3] a) O. Kwon, J. Kang, S. Kim, T. Yoon, *Adv. Funct. Mater.* **2025**, *35*, 2420474; b) M. Li, B. Wang, J. Ma, Z. Wang, Y. Liang, Z. Wang, L. Zhang, Y. Tang, Q. Huang, J. Huang, *Adv. Energy Mater.* **2024**, *14*, 2303156.
[4] Y.-G. Lee, S. Fujiki, C. Jung, N. Suzuki, N. Yashiro, R. Omoda, D.-S. Ko, T. Shiratsuchi, T. Sugimoto, S. Ryu, J. H. Ku, T. Watanabe, Y. Park, Y. Aihara, D. Im, I. T. Han, *Nat. Energy* **2020**, *5*, 299.
[5] D. Gu, H. Kim, J.-H. Lee, S. Park, *J. Energy Chem.* **2022**, *70*, 248.
[6] a) X. Xing, Y. Li, S. Wang, H. Liu, Z. Wu, S. Yu, J. Holoubek, H. Zhou, P. Liu, *ACS Energy Lett.* **2021**, *6*, 1831; b) S. E. Sandoval, J. A. Lewis, B. S. Vishnugopi, D. L. Nelson, M. M. Schneider, F. J. Q. Cortes, C. M. Matthews, J. Watt, M. Tian, P. Shevchenko, P. P. Mukherjee, M. T. McDowell, *Joule* **2023**, *7*, 2054; c) Y. Wang, Y. Liu, M. Nguyen, J. Cho, N. Katyal, B. S. Vishnugopi, H. Hao, R. Fang, N. Wu, P. Liu, P. P. Mukherjee, J. Nanda, G. Henkelman, J. Watt, D. Mitlin, *Adv. Mater.* **2023**, *35*, 2206762; d) J. Kim, S. Lee, J. Kim, J. Park, H. Lee, J. Kwon, S. Sun, J. Choi, U. Paik, T. Song, *Carbon Energy* **2024**, *6*, 610.
[7] R. Peter, M. Petravic, *J. Phys. Chem. C* **2021**, *125*, 25290.
[8] G. Lorang, M. D. Cunha Belo, A. M. P. Simões, M. G. S. Ferreira, *J. Electrochem. Soc.* **1994**, *141*, 3347.
[9] J. S. Yoon, D. W. Liao, S. M. Greene, T. H. Cho, N. P. Dasgupta, D. J. Siegel, *ACS Appl. Mater. Interfaces* **2024**, *16*, 18790.
[10] L. Dupont, S. Grugeon, S. Laruelle, J. M. Tarascon, *J. Power Sources* **2007**, *164*, 839.
[11] a) A. L. Davis, E. Kazyak, D. W. Liao, K. N. Wood, N. P. Dasgupta, *J. Electrochem. Soc.* **2021**, *168*, 070557; b) Y. Wang, V. Raj, K. G. Naik, B. S. Vishnugopi, J. Cho, M. Nguyen, E. A. Recker, Y. Su, H. Celio, A. Dolocan, Z. A. Page, J. Watt, G. Henkelman, Q. H. Tu, P. P. Mukherjee, D. Mitlin, *Adv. Mater.*, *37*, 2410948.
[12] J. A. Lewis, S. E. Sandoval, Y. Liu, D. L. Nelson, S. G. Yoon, R. Z. Wang, Y. Zhao, M. K. Tian, P. Shevchenko, E. Martínez-Pañeda, M. T. McDowell, *Adv. Energy Mater.* **2023**, *13*, 12.
[13] Y. Huang, Y. Zhang, R. Wu, B. Shao, R. Deng, R. Das, F. Han, *ACS Energy Lett.* **2024**, *9*, 3409.
[14] R.-H. Jung, H. Tsuchiya, S. Fujimoto, *Corros. Sci.* **2012**, *58*, 62.
[15] M. Biesinger, C. Brown, J. Mycroft, R. Davidson, N. McIntyre, *Surface and Int. analysis* **2004**, *36*, 1550.

[16] S. D. Giri, A. Sarkar, *J. Electrochem. Soc.* **2016**, *163*, H252.
[17] a) N. S. McIntyre, M. G. Cook, *Anal. Chem.* **1975**, *47*, 2208; b) T. Ghodselahi, M. A. Vesaghi, A. Shafiekhani, A. Baghizadeh, M. Lameii, *Appl. Surf. Sci.* **2008**, *255*, 2730.
[18] J. Qian, W. A. Henderson, W. Xu, P. Bhattacharya, M. Engelhard, O. Borodin, J.-G. Zhang, *Nat. Commun.* **2015**, *6*, 6362.
[19] B. Lelotte, C. A. F. Vaz, L. Xu, C. N. Borca, T. Huthwelker, V. Pelé, C. Jordy, L. Gubler, M. El Kazzi, *ACS Appl. Mater. Int.* **2025**, *17*, 14645.
[20] C. Vogel, C. Rivard, V. Wilken, A. Muskolus, C. Adam, *Ambio* **2018**, *47*, 62.
[21] C. Yu, Y. Li, W. Li, K. R. Adair, F. Zhao, M. Willans, J. Liang, Y. Zhao, C. Wang, S. Deng, R. Li, H. Huang, S. Lu, T.-K. Sham, Y. Huang, X. Sun, *Energy Storage Mater.* **2020**, *30*, 238.
[22] A. P. Woodhead, A. Gutiérrez-Sosa, P. Martinez-Escolano, G. Thornton, *Phys. Rev. B* **2004**, *70*, 193404.
[23] R. K. Szilagyi, P. Frank, S. DeBeer George, B. Hedman, K. O. Hodgson, *Inorg. Chem.* **2004**, *43*, 8318.
[24] M. Abe, F. Kaneko, N. Ishiguro, T. Kubo, F. Chujo, Y. Tamenori, H. Kishimoto, Y. Takahashi, *J. Phys. Chem. C* **2022**, *126*, 14047.
[25] M. Kiguchi, K. Saiki, *J. o Surface Sci. and Nanotech.* **2004**, *2*, 191.
[26] a) Y. Sun, K. Suzuki, K. Hara, S. Hori, T.-a. Yano, M. Hara, M. Hirayama, R. Kanno, *J. Power Sources* **2016**, *324*, 798; b) A. Banerjee, H. Tang, X. Wang, J.-H. Cheng, H. Nguyen, M. Zhang, D. H. Tan, T. A. Wynn, E. A. Wu, J.-M. Doux, *ACS Appl. Mater. Int.* **2019**, *11*, 43138.
[27] W. Li, J. Liang, M. Li, K. R. Adair, X. Li, Y. Hu, Q. Xiao, R. Feng, R. Li, L. Zhang, *Chem. Mater.* **2020**, *32*, 7019.
[28] H. Konishi, M. Yamashita, H. Uchida, i. M. Jun, *Mater. Trans.* **2005**, *46*, 329.
[29] Y. Wang, X. Feng, Y. Xiong, S. Stoupin, R. Huang, M. Zhao, M. Xu, P. Zhang, J. Zhao, H. c. D. Abruña, *ACS Appl. Mater. Int.* **2020**, *12*, 17396.
[30] D. A. Riego, V. M. Sbarato, J. J. Leani, H. J. Sánchez, I. Carlomagno, R. D. Perez, *Anal. Chim. Acta* **2024**, *1329*, 343201.
[31] M. Tromp, J. Moulin, G. Reid, J. Evans, AIP Conference Proceedings **2007**, *882*, 699.
[32] H. C. Wells, K. H. Sizeland, R. L. Edmonds, W. Aitkenhead, P. Kappen, C. Glover, B. Johannessen, R. G. Haverkamp, *ACS Sus. Chem. Eng.* **2014**, *2*, 1864.
[33] B. Zhou, I. Stoševski, A. Bonakdarpour, D. P. Wilkinson, *ACS Appl. Energy Mater.* **2023**, *6*, 6890.
[34] E. E. Morgan, H. A. Evans, K. Pilar, C. M. Brown, R. J. Clément, R. Maezono, R. Seshadri, B. Monserrat, A. K. Cheetham, *Chem. Mater.* **2022**, *34*, 4029.
[35] R. J. Gillespie, E. A. Robinson, *Can. J. Chem.* **1963**, *41*, 2074.
[36] K. Chavez, D. Hess, *J. Electrochem. Soc.* **2001**, *148*, G640.
[37] M. C. Biesinger, *Surf. Int. Anal.* **2017**, *49*, 1325.
[38] Z. Gong, C. Lian, P. Wang, K. Huang, K. Zhu, K. Ye, J. Yan, G. Wang, D. Cao, *Energy & Env. Mat.* **2022**, *5*, 1270.
[39] K. Yu, J. Chen, X. Xie, K. Lin, J. Li, Z. Shi, *Surfaces and Int.* **2022**, *34*, 102326.
[40] S. Wang, S. Li, X. Chen, Q. Yin, W. Zhang, Y. Ning, G. Zhang, Q. Fu, *J. Am. Chem. Soc.* **2025**.
[41] a) G. G. Eshetu, T. Diemant, S. Grugeon, R. J. Behm, S. Laruelle, M. Armand, S. Passerini, *ACS Appl. Mater. Int.* **2016**, *8*, 16087; b) W. Yu, Z. Yu, Y. Cui, Z. Bao, *ACS Energy Lett.* **2022**, *7*, 3270.
[42] Y. Diao, K. Xie, S. Xiong, X. Hong, *J. Electrochem. Soc.* **2012**, *159*, A1816.
[43] a) G. Deroubaix, P. Marcus, *Surf. Interface Anal.* **1992**, *18*, 39; b) K. M. Abraham, S. M. Chaudhri, *J. Electrochem. Soc.* **1986**, *133*, 1307.
[44] J. Ghijsen, L. H. Tjeng, J. van Elp, H. Eskes, J. Westerink, G. A. Sawatzky, M. T. Czyzyk, *Phys. Rev. B* **1988**, *38*, 11322.
[45] V. Krylova, M. Andrulevičius, *Int. J.o Photoenergy* **2009**, *2009*, 304308.
[46] P. Thörnig, *J. o large-scale res. facilities JLSRF* **2021**, *7*, A182.